

Modeling and performance analysis of the LUVOIR coronagraph instrument

Roser Juanola-Parramon,^{a,b} Neil T. Zimmerman[©],^a Laurent Pueyo,^c
Matthew Bolcar,^a Qian Gong[©],^a Tyler Groff[©],^a John Krist,^d
Aki Roberge[©],^a Garreth Ruane[©],^d and Christopher Stark^a

^aNASA Goddard Space Center, Greenbelt, Maryland, United States

^bUniversity of Maryland, Baltimore County, Baltimore, Maryland, United States

^cSpace Telescope Science Institute, Baltimore, Maryland, United States

^dCalifornia Institute of Technology, Jet Propulsion Laboratory,
Pasadena, California, United States

Abstract. Future space missions such as the Large UV/Optical/Infrared Surveyor (LUVOIR) and the Habitable Exoplanet Observatory, when equipped with coronagraphs with active wavefront control to suppress starlight, will allow the discovery and characterization of habitable exoplanets. The Extreme Coronagraph for Living Planetary Systems (ECLIPS) is the coronagraph instrument on the LUVOIR Surveyor mission concept, an 8- to 15-m segmented telescope. ECLIPS is split into three channels, namely, UV (200 to 400 nm), optical (400 to 850 nm), and near IR (850 nm to 2 μm), with each channel equipped with two deformable mirrors for wavefront control, a suite of coronagraph masks, a low-order/out-of-band wavefront sensor, and separate science imagers and spectrographs. The apodized pupil Lyot coronagraph and the vector vortex coronagraph are the baselined mask technologies for ECLIPS to enable the required 10^{-10} contrast for observations in the habitable zones of nearby stars for LUVOIR-A (15-m telescope) and LUVOIR-B (8-m telescope), respectively. Their performance depends on active wavefront sensing and control, as well as metrology subsystems to compensate for aberrations induced by segment errors (e.g., piston and tip/tilt), secondary mirror misalignment, and global low-order wavefront errors. Here, we present the latest results of the simulation of these effects for the LUVOIR coronagraph instrument and discuss the achieved contrast for exoplanet detection and characterization after closed-loop wavefront estimation and control algorithms have been applied. Finally, we show simulated observations using high-fidelity spatial and spectral input models of complete planetary systems generated with the Haystacks code framework. © The Authors. Published by SPIE under a Creative Commons Attribution 4.0 International License. Distribution or reproduction of this work in whole or in part requires full attribution of the original publication, including its DOI. [DOI: [10.1117/1.JATIS.8.3.034001](https://doi.org/10.1117/1.JATIS.8.3.034001)]

Keywords: high-contrast imaging; direct detection; coronagraphs; exoplanets; modeling; LUVOIR.

Paper 22017G received Feb. 7, 2022; accepted for publication Jun. 17, 2022; published online Jul. 19, 2022.

1 Introduction

Decades of exoplanet observations using a variety of techniques have revealed a universe filled with exoplanets of an astounding variety. While some of these planetary systems may resemble our own, others are vastly different, i.e., evaporated cores of gas giants, gaseous sub-Neptune planets, and giant planets on retrograde, eccentric orbits. But, we have yet to answer, do other Earth-like planets exist? And do they provide an opportunity for life to arise elsewhere? Answering these questions, by searching for and characterizing other potentially Earth-like worlds around Sun-like stars, is within our grasp for the first time.

Indeed, conducting this ambitious experiment is one of the key recommendations of the 2018 National Academies of Sciences' Exoplanet Science Strategy Report,¹ and the primary

*Address all correspondence to Roser Juanola-Parramon, rosjer.juanola@nasa.gov

recommendation of the recent Astro2020 decadal survey:² Pathways to Discovery in Astronomy and Astrophysics for the 2020s. The decadal survey states that “inspired by the vision of searching for signatures of life on planets outside of the Solar System, and by the transformative capability such a telescope would have for a wide range of astrophysics, the survey recommends that the first mission to enter this program is a large (6-m aperture) infrared/optical/ultraviolet (IR/O/UV) space telescope. The scientific goals of this mission, when achieved, have the potential to profoundly change the way that human beings view our place in the universe.” Specifically, the decadal survey committee concludes that “A high-contrast direct imaging mission with a target off-axis inscribed diameter of ~6 m provides an appropriate balance between scale and feasibility. Such a mission will provide a robust sample of 25 atmospheric spectra of potentially habitable exoplanets, will be a transformative observatory for general astrophysics, and given optimal budget profiles it could launch by the first half of the 2040 decade.”

The Large UV/Optical/Infrared Surveyor³ (LUVOIR) is one of the four mission concepts submitted to the Astro2020 decadal survey, and it has the specific capability to detect and characterize habitable exoplanets, as well as to gain access to a large range of astrophysics. In light of the decadal recommendation, we describe the point design from the end of the concept study in 2019. Our hope is that the material here-in serves as a starting point for the technology maturation phase.

2 Large UV-Optical-Infrared Surveyor

LUVOIR is a large aperture, serviceable, multi-wavelength space observatory with science goals that would enable transformative advances across a broad range of astrophysics. Two mission concepts have been studied: LUVOIR-A, a 15-m on-axis segmented aperture, and LUVOIR-B, an 8-m off-axis segmented aperture.

Optically, LUVOIR-A and LUVOIR-B, shown in Fig. 1(a), are designed as a three-mirror anastigmat system with a fourth fine steering mirror located at the real exit pupil of the optical telescope element, which enables a wide field-of-view that can be accessed by its instruments, and ultra-fine pointing stability. The LUVOIR-A concept has four instruments: the High Definition Imager (HDI), the LUVOIR Ultraviolet Multi-Object Spectrograph (LUMOS),⁴ the UV spectro-polarimeter POLLUX⁵ and the Extreme Coronagraph for Living Planetary Systems (ECLIPS),⁶⁻⁸ while LUVOIR-B has three instruments: HDI, LUMOS, and ECLIPS.

The key telescope parameters for LUVOIR are given in Table 1. Notably, with its off-axis design and inscribed primary mirror diameter of 6.7 m, the LUVOIR-B design is in line with the recommendations of the Astro2020 Decadal Report.

The LUVOIR science goals are very ambitious, and require detecting and characterizing some of the faintest exoplanets ever imaged in sample sizes that can allow for meaningful statistical queries. The exoplanet detection yields⁹ for the two versions of LUVOIR are shown in

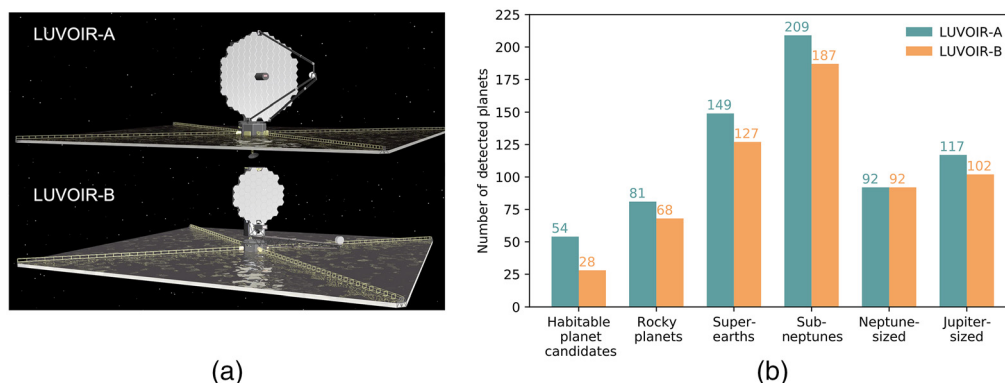


Fig. 1 (a) The LUVOIR-A and LUVOIR-B mission concepts. (b) Exoplanet discovery yields based on a two year census of Earth-like exoplanets with LUVOIR-A and LUVOIR-B.

Table 1 LUVOIR telescope specifications.

Telescope	LUVOIR-A	LUVOIR-B
Circumscribing perimeter diameter (m)	15.005	7.994
Inscribing perimeter diameter (m)	13.502	6.718
Circumscribing obscuration diameter (m)	1.427	N/A
Inscribing obscuration diameter (m)	1.235	N/A
Segment size (flat-to-flat) (m)	1.2225	0.955
Gap size (m)	0.006	0.006
Number of segments	120	55
Collecting area (m ²)	155.20	43.419

Fig. 1(b) from an initial two-year survey optimized for habitable planet candidates. Concurrent to the habitable planet candidates, non-habitable planets are detected during the survey.

3 Extreme Coronagraph for Living Planetary Systems

The complexity of imaging exoplanets resides in the extreme ratio in flux with respect to their parent star, in addition to their sub-arcsecond angular proximity. For this reason, we require large telescope apertures with extreme sensitivity equipped with coronagraph instruments for starlight suppression.

The coronagraph instrument on LUVOIR, ECLIPS, is split into three channels via dichroics: UV (200 to 400 nm), optical (400 to 850 nm), and NIR (850 nm to 2 μ m). This division is driven by the three different detector technologies needed in UV, visible, and near IR because to date there is no single detector technology that covers this entire spectral range.⁷ Each channel is equipped with two deformable mirrors (DMs) for wavefront control, a suite of coronagraph masks, and separate science imagers and spectrographs. Simultaneous observations in two channels at a time are expected and accounted for in the reported total exposure times. It is assumed that the third channel will provide wavefront sensing, although observations in all three channels simultaneously may become possible in the future with technological improvements. In addition, all three channels also have a low-order/out-of-band wavefront sensor that uses light reflected from the focal plane mask (FPM) to sense pointing errors and wavefront drifts that originate from secondary mirror motion or absolute pointing error of the observatory.

The segmented coronagraph design and analysis (SCDA) study,¹⁰ led by NASA's Exoplanet Exploration Program, has shown that several coronagraph mask technologies are compatible with segmented primary mirrors.¹¹ The mask types with the most mature designs for consideration in the LUVOIR study were the vector vortex coronagraph (VVC) and the apodized pupil Lyot coronagraph (APLC).

In the presence of even a modest central obscuration, as is the case for the LUVOIR-A telescope ($\sim 10\%$ of the diameter), the APLC provides the best overall performance.^{9,12–14} Therefore, most LUVOIR-A ECLIPS observing modes rely on a suite of APLC masks optimized for various ranges of angular separation. The LUVOIR-B ECLIPS concept, on the other hand, makes use of the VVC's superior performance on unobscured segmented pupils^{15,16} [in terms of inner working angle (IWA) and core throughput]. Both the A and B ECLIPS concepts carry slots for alternative mask types to reduce risk, since different mask technologies tend to have complementary performance sensitivities. As an example, the phase-induced amplitude apodization (PIAA) coronagraph^{17–19} is another promising coronagraph architecture for LUVOIR-B, though we do not analyze the LUVOIR-B PIAA performance in this paper.

The goal of ECLIPS is to perform direct imaging and characterization of potentially habitable extrasolar planets. The detectability of exoplanets in long coronagraph exposures depends on

both the level of contrast achieved in the high-contrast region or dark zone of the focal plane, and on the core throughput of the coronagraph at the apparent separation of the planets located between the minimum and maximum angular separations that define the dark zone, beyond the so-called IWA and outer working angle (OWA). Given that the flux ratio between an Earth-like exoplanet and its parent star will be of the order of 10^{-10} in visible light, ECLIPS must achieve starlight suppression of at least 10^{-10} . Even after achieving such a deep contrast, the number of detectable exoplanets depends strongly on the IWA of this dark search zone.²⁰ For this reason, the ECLIPS concepts for LUVOIR-A and B are designed to access angular separations as low as, respectively, $3.5 \lambda/D$ and $2 \lambda/D$ from the star (where λ is the wavelength and D is the diameter of the telescope) equivalent to 34 and 36 mas on the sky at a wavelength of $\lambda = 700$ nm, with an PSF core throughput, this is the fraction of a planet’s light incident on the primary mirror that ends up in the core of the PSF (the region with values $>50\%$ of the PSF peak), $>15\%$.

Here, we present the numerical model of the ECLIPS instrument for both LUVOIR-A and LUVOIR-B, which we use to evaluate the performance of the instrument as well as to simulate the effects of wavefront aberrations and their impact on coronagraph performance. First, in Sec. 4, we provide an overview of the coronagraph designs for ECLIPS. In Sec. 5, we evaluate the general performance of these designs under the assumption of a perfect telescope. In Sec. 6, we evaluate the sensitivity to telescope aberrations by simulating quasi-static and dynamic aberrations, as well as the wavefront sensing and control required to mitigate their effects. Finally, in Sec. 7, we present the first simulated observation of a planetary system with the LUVOIR-A ECLIPS instrument.

4 Coronagraph Designs for ECLIPS

The two baseline coronagraph designs envisioned for ECLIPS are an APLC for LUVOIR-A, and a VVC for LUVOIR-B. Tables 2 and 3 summarize the key parameters for ECLIPS for LUVOIR-A and LUVOIR-B, respectively. It can be noticed that the two types of coronagraph differ in terms of instantaneous bandpass, which results in an increase of the number of filters required for

Table 2 LUVOIR-A ECLIPS specifications.

LUVOIR-A	N filt	Bandpass (%)	Min λ (nm)	Max λ (nm)	APOD	IWA λ/D	OWA λ/D	IWA (mas) @ min λ	IWA (mas) @ max λ	OWA (mas) @ min λ	OWA (mas) @ max λ
UV	16	10	210	500	Narrow	4	12	11.6	34.7	27.5	82.5
					Med	6	20	17.3	57.8	41.3	137.5
					Wide	12	40	34.7	115.5	82.5	275.0
Vis	28	10	542	981	Narrow	3.5	12	26.1	89.4	47.2	161.9
					Med	6	20	44.7	149.1	80.9	269.8
					Wide 1	12	40	89.4	298.1	161.9	539.6
					Wide 2	20	64	149.1	477.0	269.8	863.3
					VVC	2	64	14.9	477.0	27.0	863.3
NIR	25	10	1052	1905	Narrow	3.5	12	50.6	173.6	91.7	314.3
					Med	6	20	86.8	289.3	157.2	523.9
					Wide 1	12	40	173.6	578.6	314.3	1047.8
					Wide 2	20	64	289.3	925.8	523.9	1676.5
					VVC	2	64	28.9	925.8	52.4	1676.5

Table 3 LUVOIR-B ECLIPS specifications.

LUVOIR-B	N filt	Bandpass (%)	Min	Max	APOD	IWA λ/D	OWA λ/D	IWA	IWA	OWA	OWA
			λ (nm)	λ (nm)				(mas) @ min λ	(mas) @ max λ	(mas) @ min λ	(mas) @ max λ
UV	5	20	222	486	VVC	2	28	11.5	25.1	160.5	350.9
Vis	4	20	572	985	VVC	2	28	29.5	50.8	413.4	711.7
NIR	4	20	1111	1913	VVC	2	28	57.3	98.7	802.7	1382.0

LUVOIR-A compared to LUVOIR-B. To access the different bandpasses, each of the three channels features a post-coronagraph imager with a filter mechanism. The large compliment of filters is accommodated by a number of small filter wheels in series. For example, the ECLIPS-A visible channel filter selection mechanism consists of five wheels in series, each with seven element positions, one of which is an “open” slot to allow the beam to pass through and reach the wheel behind it. This provides 30 (7×5 positions— five open positions) for the required 28 filters. The two remaining slots are used for a “closed” position for dark calibration and a neutral density filter.

The optical design for both cases is identical and is shown unfolded in Fig. 2. This simplified version has been derived from the high fidelity LUVOIR optical design.²¹

We can divide the optical layout into two main parts: the wavefront control optics and the coronagraph optics. The wavefront control optics are comprised of two DMs required to optimize the coronagraph performance by correcting wavefront aberrations, as well as for apodization for the VVC design. The DM1 is in the pupil plane while DM2 is at a distance z_{DM} from DM1. For LUVOIR, the current design requires 128×128 actuators per DM to perform active wavefront control up to an OWA of $64 \lambda/D$, which provides access to outer giant planets. However, for practical reasons (computational resources and maximum OWA of the masks used in this article) the simulations presented here assume 64×64 actuators per DM as the larger OWA evaluated is $28 \lambda/D$. In principle, one set of VVC masks could operate at arbitrary large OWA as long as the DM actuator density is high enough. For APLC on the other hand, increases in OWA require a trade-off in IWA and throughput. For the specific coronagraphs masks used here, the reduced actuator density (64×64) will not have a significant impact on performance predictions of the wavefront control system.

The coronagraph optics include the off-axis parabolic mirrors (OAPs) (in Fig. 2 represented as lenses) and the coronagraph masks: an apodizer, a FPM and a Lyot stop. Although the masks are different, the principle of operation is the same for APLC and VVC: the star light (orange) enters the system on-axis. The combination of DMs and apodizer modulate the on-axis complex

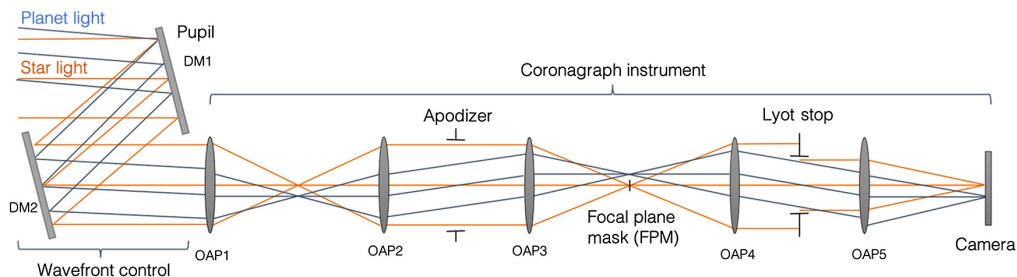


Fig. 2 Optical layout and principle of operation of the ECLIPS instrument. Starlight (orange) and planet light (blue) enter the optical system on-axis and off-axis, respectively. The wavefront control optics (DM1 and DM2) apodize the incoming light and/or correct for telescope aberrations. OAP1 and OAP2 collimate the beam and relay the pupil image to the apodizer. The apodizer further modulates the incoming light, before an OAP focuses it on the FPM. The stellar PSF is highly suppressed in a dark zone prescribed by the apodizer and/or DMs while off-axis planet light propagates through the system, attenuated only by the apodizer and Lyot stop.

field such that the diffracted starlight in the FPM plane is concentrated outside the coronagraph dark zone (IWA-OWA region). The FPM blocks the on-axis light while off-axis planet light propagates through the system. The Lyot stop further suppresses residual starlight.

4.1 Apodized Pupil Lyot Coronagraph

Following Fig. 2, at the relayed telescope pupil (apodizer plane), the field corresponding to the collimated on-axis starlight is modulated in amplitude by the apodizer, in this case, a binary-valued transmission pattern. The light is then focused onto the FPM, which occults the core of the stellar PSF. The diameter of the FPM determines the IWA of the coronagraph: an off-axis source situated outside the angular scale of the FPM propagates onward with minimal distortion. The beam is then re-collimated and modulated by the Lyot stop, before the final focus onto the detector. The apodizer transmission pattern is numerically optimized—with knowledge of the downstream FPM and Lyot stop—to produce a specified dark zone (contrast and spatial extent) while maximizing the transmission of the off-axis planet.²²

Figure 3 shows the APLC masks for LUVOIR-A. Two sets of mask are shown: LUVOIR-A APLC narrow and wide, which cover a dark zone from 3.5 to $12 \lambda/D$, and 7 to $27 \lambda/D$, respectively. The narrow angle set of masks used here are designed for a 10% bandpass, whereas the wide angle masks are designed for an 18% bandpass.

One of the main advantages of the APLC is its adaptability to arbitrary telescope aperture shapes.¹³ In our case, the primary mirror segment gaps and struts are taken into account by the apodizer profile. This relaxes the demands on stroke and actuator density placed on the DM components in the wavefront control system, which can instead be dedicated to the compensation of aberrations and maintenance of the dark zone. In the current LUVOIR-A optical design, the separation between DMs is set to $z_{DM} = 0.8$ m, which is the minimum separation to achieve simultaneous correction of amplitude and phase errors. This separation is driven by the Talbot effect.^{21,23}

4.2 Vector Vortex Coronagraph

For the VVC, we assume a DM-only apodized design,²⁴ i.e., the DMs are actively used to create the desired apodization pattern. Following Fig. 2, the complex field corresponding to the starlight is modulated with the DMs and a circular aperture located at the apodizer plane. The light is then focused onto the focal plane phase mask, which suppresses the diffraction from the central

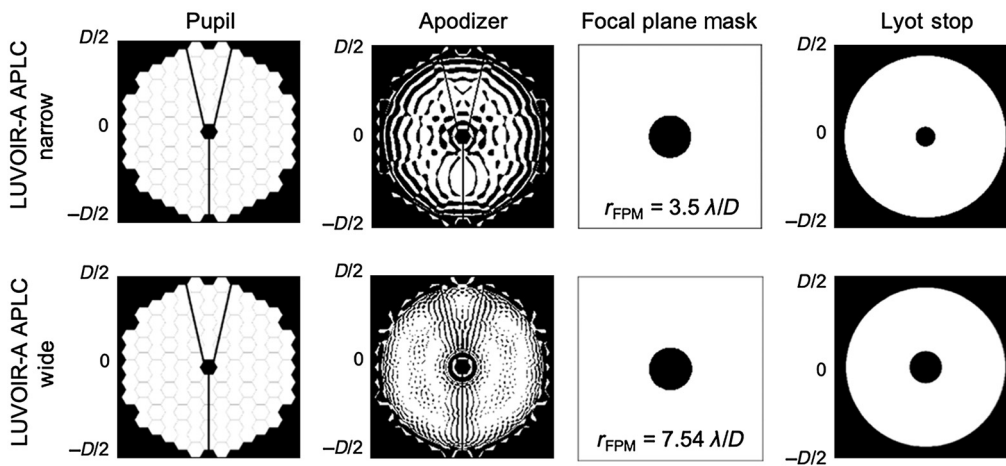


Fig. 3 LUVOIR-A pupil (left) and APLC masks for a narrow angle design (top) and wide angle design (bottom). The apodizer transmission patterns are numerically optimized – with knowledge of the downstream FPM and Lyot stop—to produce a specified dark zone while maximizing the transmission of the off-axis planet. All the masks are binary, and the FPM is a sharp edge occulter mask.

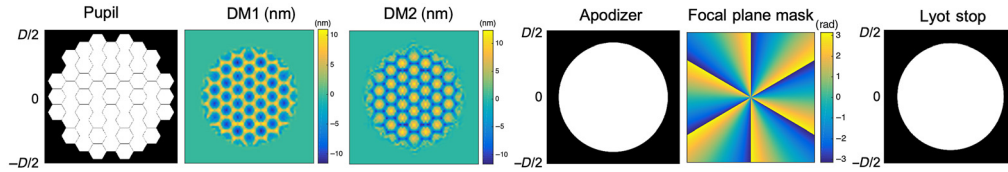


Fig. 4 LUVOIR-B pupil (left) and vector vortex DM-only apodization masks. The telescope pupil is reshaped by the DMs (DM1 and DM2). The apodizer is a circular aperture (diameter 0.84 D). The FPM is a charge six vortex phase mask, assumed achromatic for the simulations presented in this study. The Lyot stop is a circular aperture with a diameter 0.82D.

obscuration. The FPM has a complex transmittance given by $\exp(il\theta)$, where θ is the azimuthal angle and l is the charge. The DM shapes and masks for this design are shown in Fig. 4.

The apodizer is a circular aperture with a diameter 84% of the circumscribed diameter of the LUVOIR-B pupil. The FPM is a charge six vortex and the Lyot stop is 82% of the circumscribed diameter of the LUVOIR-B pupil. The DM shapes in this design have been optimized at a given DMs separation, and this separation is prescribed by $z_{DM} = R^2/(F_0\lambda)$, where R is the pupil radius, λ is the wavelength, and F_0 is the Fresnel number. The Fresnel number is set to $F_0 = 550$ for optimal performance of the coronagraph.²³ This corresponds to a DM separation of ~ 2 m. Finally, this design provides a 20% bandpass, but the simulations presented here assume 10% for consistency with the LUVOIR-A APLC design.

5 Evaluation of Coronagraph Designs

To study the performance of the LUVOIR-A APLC and its sensitivity to telescope aberrations we developed a model using a combination of the Python version of the PROPER Optical Propagation Library²⁵ and fast Fourier transform/matrix Fourier transforms (FFTs/MFTs).²⁶ Our prescription is based on the ECLIPS Zemax optical design,²⁷ but some simplifications have been made to fold the optical information into PROPER. Because PROPER does not model OAPs, all the OAPs have been replaced by ideal lenses and their focal length modified accordingly as $f_{\text{lens}} = f_{\text{OAP}}/2$, where f_{OAP} is the parent focal length of the OAP. Also, the model assumes the primary mirror is unpowered, and we artificially compress the input beam to match the size of the optics from the pupil plane (DM1) as $D_{\text{pupil}} = D_{\text{telescope}}/300$ for LUVOIR-A, and $D_{\text{pupil}} = D_{\text{telescope}}/160$ for LUVOIR-B. For the DMs, each actuator is represented by the default influence function, which describes the deformation of the mirror surface when a single actuator is pistoned above surrounding actuators, distributed with the PROPER software package. We note this actuator response model makes an ideal assumption that the surface deformations can be obtained by linear superposition. Future studies may account for non-ideal interactions between neighboring actuators.

Given that the region of interest for coronagraph instruments for exo-Earth detection and characterization is near the IWA, we concentrate our analysis on the LUVOIR-A APLC narrow angle masks and VVC masks. Hence, unless otherwise specified, we will be referring to the APLC narrow angle masks as APLC masks. Because typical stellar flux peaks in the visible and decreases rapidly in the UV, we expect exposure times to be minimized at visible wavelengths. In the near-infrared, while the stellar flux is high, the IWA is larger, as well as the size of the PSF core resulting in enhanced exozodiacal light. Hence, in this paper, we only evaluate the visible channel of the coronagraph instrument.

The nominal contrast for the LUVOIR-A and LUVOIR-B coronagraph designs is shown in Fig. 5, as a function of angular separation in units of λ/D . For this simulation, we have assumed nine wavelengths per 10% bandpass, the effect of which can be clearly seen in the streaking of the diffraction pattern outside the OWA for the VVC design. For LUVOIR-A, the contrast is more uniform within the dark zone, due to the fact that the apodizer accounts for the segment gaps and struts. For LUVOIR-B, one can notice the presence of diffraction features within the dark zone, located at the harmonic spatial frequencies associated to the segmentation pattern of the aperture. These diffraction features are due to the fact that the DM apodization is intrinsically

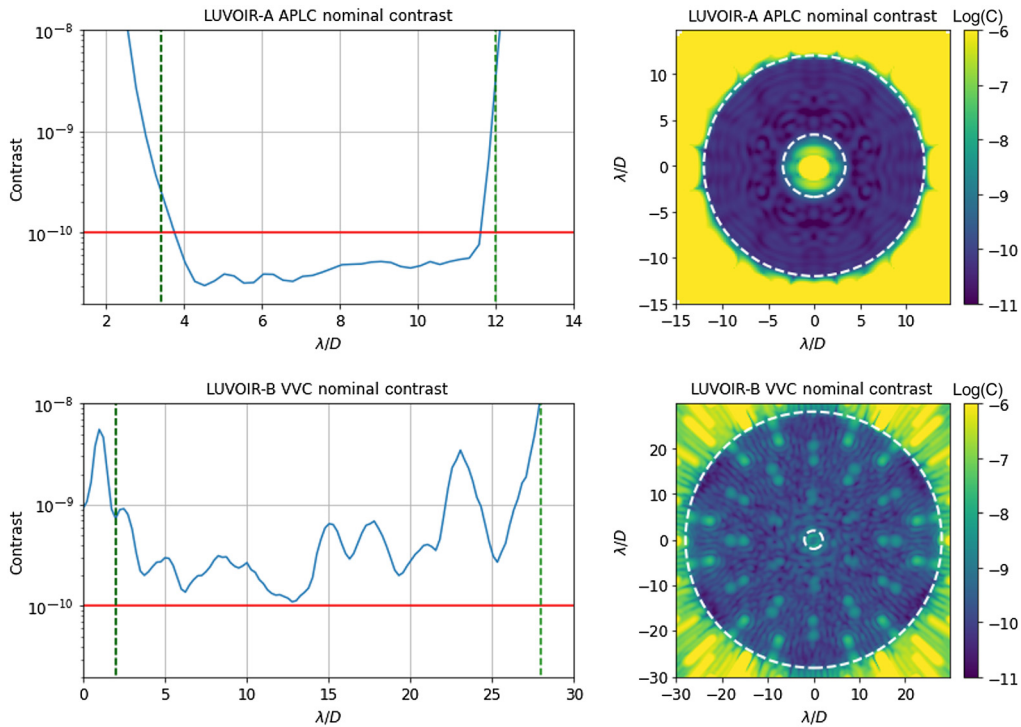


Fig. 5 Broadband PSF in units of contrast (right) and the PSF's azimuthal average (left) for LUVOIR-A APLC (top) and LUVOIR-B VVC (bottom), for a 10% bandpass. The dashed white circles indicate the IWA and OWA at the central wavelength.

chromatic. As a consequence, the nulling of the on-axis plane wave degrades toward the ends of the bandpass. In other words, the VVC dark zone of a segmented aperture is never as clean as a VVC for a monolithic mirror.

5.1 Core Throughput

We calculate the coronagraph core throughput as the fraction of light from a planet within the core of its off-axis PSF, which is defined as the region circumscribed by its half-max contour. This metric ignores losses from filters, reflections, dichroics, etc., but accounts for coronagraphic mask losses (apodizer, Lyot stop, and FPM) as well as distortion to the off-axis PSF caused by those masks and the DMs.

Figure 6(a) compares the core throughput of the LUVOIR-A APLC Narrow angle and Wide angle masks, with the LUVOIR-B VVC. Since the LUVOIR-B VVC does not use an apodizer

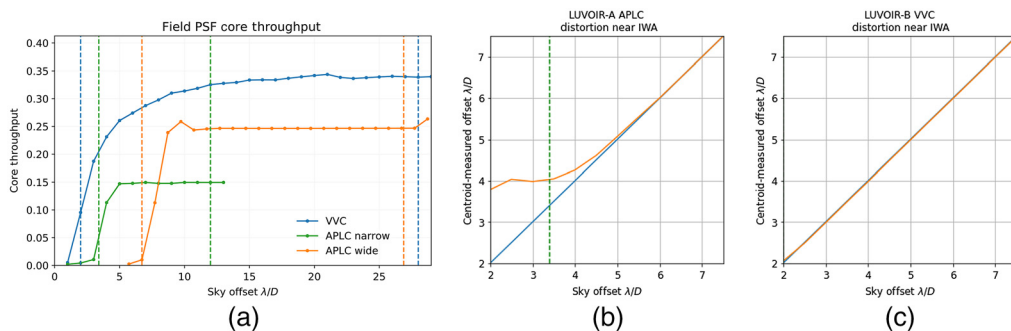


Fig. 6 Coronagraph core throughput for the LUVOIR-A APLC and LUVOIR-B VVC designs under study (a). PSF position distortion near the IWA for LUVOIR-A APLC (b) and LUVOIR-B VVC (c). The distortion near the IWA is larger in the APLC design due to the sharper edges of the occulting FPM. The diagonal blue line is a $m = 1$ slope for reference.

mask and has a transmissive FPM, its PSF core throughput is significantly higher, more noticeably at small angular separations. For LUVOIR-A, although the core throughput for the narrow angle set of masks reaches 15%, we can see a steep increase when switching to the wide angle masks. This effect is due to the APLC apodizer: the narrow angle apodizer is more opaque, which can be observed in Fig. 3.

5.2 Distortion Near the IWA

Close to the IWA, not only does the core throughput decrease, but the FPM introduces a distortion in the centroid of the off-axis (planet) PSF. Figure 6(b) and 6(c) shows the effect of the coronagraph near the IWA, which is evaluated as the photometric centroid of the planet PSF relative to its injected position in the field. For an APLC [Fig. 6(b)], the position distortion effect is more prominent due to the sharp edges of the opaque occulting spot FPM, whereas for a VVC [Fig. 6(c)] the distortion is barely noticeable.

5.3 Sensitivity to Stellar Diameter

Any telescope as large as LUVOIR will partially resolve the nearby stars that it targets during exoplanet surveys. The finite angular extent of an occulted star tends to degrade the dark zone around the IWA of a coronagraph. Thus, the impact of stellar diameter on the performance of a given coronagraph is an important design consideration for ECLIPS. For this reason, we systematically evaluated the sensitivity of each coronagraph type to stellar diameter, computing the intensity leakage into the dark zone of the coronagraph instrument.

To simulate stars as extended sources, we approximate them as a uniform grid of plane waves filling a disk, and incoherently average their contribution in the final image plane. The sampling of the extended source is set to seven plane waves spanning the diameter of the star. We evaluate the sensitivity at four apparent angular diameters: 0 mas (for reference), 0.5, 1, and 2 mas. For LUVOIR's exo-Earth survey, we expect the angular sizes of most targeted stars to fall in the range of 0.5 to 1 mas. Figure 7 summarizes the results of these trials. For both LUVOIR-A [Fig. 7(a)] and LUVOIR-B [Fig. 7(b)], we observe the effect of the star angular size causing starlight leakage in the dark zone near the IWA: the contrast degradation for the APLC design is of around $10\times$ for a 2 mas star, and around $3\times$ for a 1 mas star. For VVC, we obtain similar results in terms of contrast degradation near the IWA. However, it must be noticed that the VVC IWA is $2\lambda/D$, which is more aggressive.

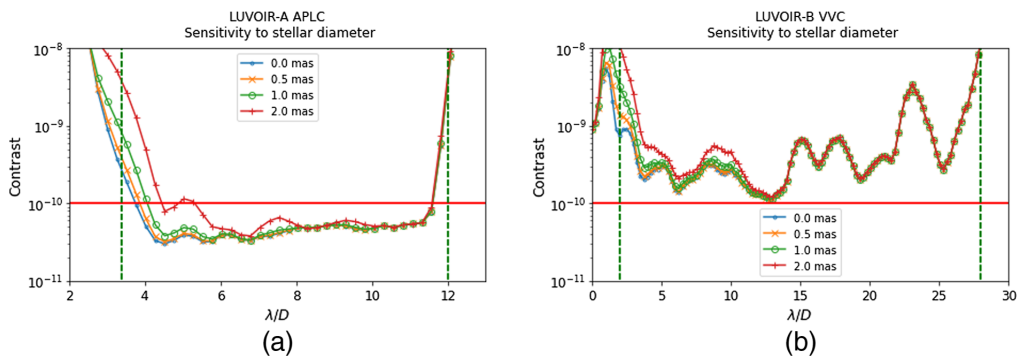


Fig. 7 Coronagraph sensitivity to stellar diameter for LUVOIR-A APLC (a) and LUVOIR-B VVC (b). We assume diameters of 0.5, 1, and 2 mas, and 0 mas (nominal contrast) is shown for reference. The red line highlights the contrast requirement of 10^{-10} for reference. The contrast degradation due to stellar leakage near the IWA is similar for both mask types.

6 Coronagraph Sensitivity to Telescope Aberrations

Up to this point, we have assumed the LUVOIR optics to be perfect while evaluating the coronagraphs. We now account for the sensitivity to optical aberrations. Any optical system will have classical wavefront errors associated with fabrication and alignment. Additionally, given the size, segmentation, and large separation between the primary and secondary mirrors, we expect to have wavefront aberrations induced by the relative movement of these two mirrors as well as misalignments at a segment level. The effects of aberrations are wavelength-dependent, hence, for the rest of this section, we have assume a 10% bandpass centered at 575 nm. Because the effects of aberrations are more prominent near the IWA, all the APLC results in this section refer to the APLC narrow angle masks. All the aberrations simulated here are included as pupil aberrations. As in Sec. 5, although the VVC design provides a 20% bandpass, the simulations presented here assume 10% for consistency with the LUVOIR-A APLC design.

For a segmented primary mirror, due to the spatial frequency of the segmentation, we expect the most stringent wavefront requirements to originate in the alignment of the segments, particularly in piston and tip/tilt.²⁸ In Fig. 8 (right), we represent the phase aberrations of each individual segment’s surface irregularity using Zernike modes. To quantify their impact, for each Zernike mode, we generate 15 independent phase error realizations of the primary mirror, each with a different total RMS wavefront error stepping from 1 to 100 picometers (pm). These realizations are generated by random normal distributions of values where each value of the distribution is the Zernike amplitude allocated to each segment. We then evaluated the mean contrast degradation in the final detector image for the two coronagraph designs. Figure 8 (right)

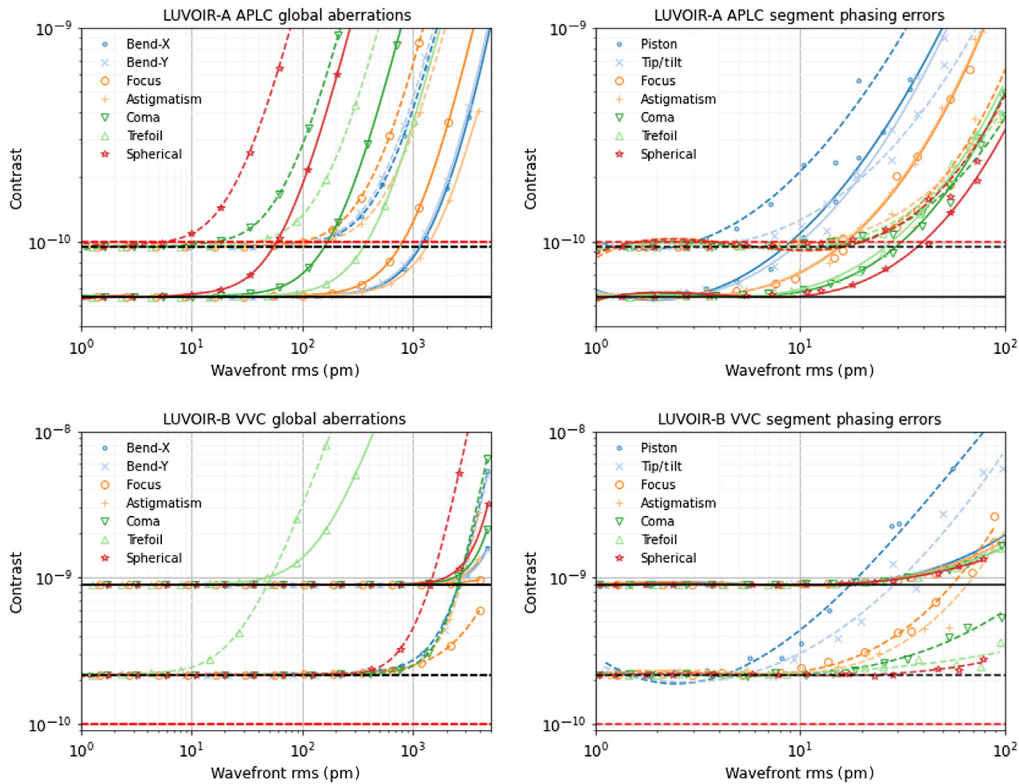


Fig. 8 Coronagraph sensitivity to global aberrations (left) and segment phasing errors (right) for the LUVOIR-A APLC design (top) and for the LUVOIR-B VVC design (bottom). Solid lines represent the average contrast in the full design dark zone, and dashed lines represent the average contrast of an annulus of $1 \lambda/D$ width centered at $4 \lambda/D$. The black lines highlight the nominal contrast in the dark zone (solid) and in the annulus (dashed). The LUVOIR designs are most sensitive to piston and tip/tilt segment phasing errors. For global aberrations, LUVOIR-A is most sensitive to spherical aberrations, whereas LUVOIR-B is most sensitive to trefoil, followed by spherical aberrations. Bend-X and Bend-Y are cylindrical aberrations across the telescope aperture. The dashed red line highlights the contrast requirement of 10^{-10} for reference.

shows the resulting contrast degradation as a function of the root-mean-square (RMS) wavefront error.

We have studied two regimes (Fig. 8): full dark zone (solid lines) and an annulus of $1 \lambda/D$ width centered at $4 \lambda/D$ (dashed lines) to capture the effects of the aberrations near the IWA, because for the APLC, the design IWA is at $3.5 \lambda/D$. For APLC, if we consider the full dark zone, the target contrast of 10^{-10} is maintained for piston and tip/tilt levels below ~ 10 pm RMS, whereas we can tolerate higher levels of wavefront RMS for subsequent Zernike modes. For the VVC design, because the nominal contrast is above 10^{-10} due to the speckles in the nominal PSF, we study the RMS level at which the contrast starts degrading. As for the APLC, the tip/tilt and piston values at which the contrast starts degrading from the nominal value are around 10-pm RMS. To disentangle the effects of the different Zernike modes, it is easier to study the contrast degradation at the $4 \lambda/D$ annulus: in both cases we confirm that the coronagraph instrument is most sensitive to segment-to-segment piston and tip-tilt errors. For APLC, the contrast degradation at the $4 \lambda/D$ annulus is more prominent than for VVC with respect to their nominal values, which is due to the fact that this annulus is closer to the design IWA for APLC than for VVC.

Global aberrations can be present at the pupil plane due to the primary mirror itself or due to misalignments of the secondary mirror, as these translate to wavefront aberrations in the form of Zernike modes at the pupil plane. Figure 8 (left) shows the contrast degradation as a function of the wavefront error for different types of global aberrations, in this case from 1- to 5-nm RMS wavefront error. For LUVOIR-A, the coronagraph is most sensitive to spherical aberrations: the contrast remains below 10^{-10} for a wavefront error below 55-pm RMS. For LUVOIR-B, the contrast starts degrading first due to trefoil (around 10-pm wavefront RMS), followed by spherical aberrations (around 1-nm wavefront RMS). However, trefoil tends to result from common three-point mounting schemes used for monolithic mirrors and is not expected to be a dominant term for LUVOIR's segmented primary mirror. Instead, the Bend-X mode associated with the deployable primary mirror's wing motion will likely be dominant. Figure 8 (bottom-left) shows the VVC to be very insensitive to this particular error term.

6.1 Active Correction of Quasi-Static Aberrations

Even with state-of-the-art telescope design assumptions, the LUVOIR concept will not rely entirely on mechanisms built into the primary mirror to align the segments to within the 10-pm tolerances suggested above. Instead, the ECLIPS instrument design—similar to the Nancy Grace Roman Space Telescope (RST) Coronagraph Instrument—relies on a wavefront control system that includes a series of two DMs to compensate for quasi-static aberrations originating in the primary mirror. To examine the capability of sensing quasi-static wavefront aberrations and correcting them with a two-DM system, we expanded the LUVOIR model to include wavefront control based on the electric field conjugation (EFC) method. The model²⁹ can perform wavefront estimation via pair-wise sensing,³⁰ which allows the estimation of the focal plane electric field from a set of intensity images captured by setting a predefined DM shape, but in this section, we have assumed perfect knowledge of the electric field at the detector plane to increase the simulation computational speed and decouple the effects of sensing error on our ability to compensate the modeled aberrations of the observatory.

As described above, the segment-to-segment errors that dominate the contrast degradation are piston and tip/tilt rather than higher-order modes. To study the effectiveness of our wavefront control system, we generated a set of wavefront error maps with equal levels of piston and tip/tilt contributions. It should be noted that in terms of total RMS wavefront error, the segment tip and tilt contributions add in quadrature.

These wavefront error maps are fed into our model, and EFC is activated. The results obtained are shown in Fig. 9 as the evolution of the contrast, averaged in the dark zone, per iteration of the optimization algorithm. It can be observed that for wavefront errors of at least up to 7-nm RMS, our wavefront control system can correct the wavefront error and drive the dark zone to values below the 10^{-10} target for APLC [Fig. 9(a)], and to the nominal contrast for VVC [Fig. 9(b)], after three control iterations.

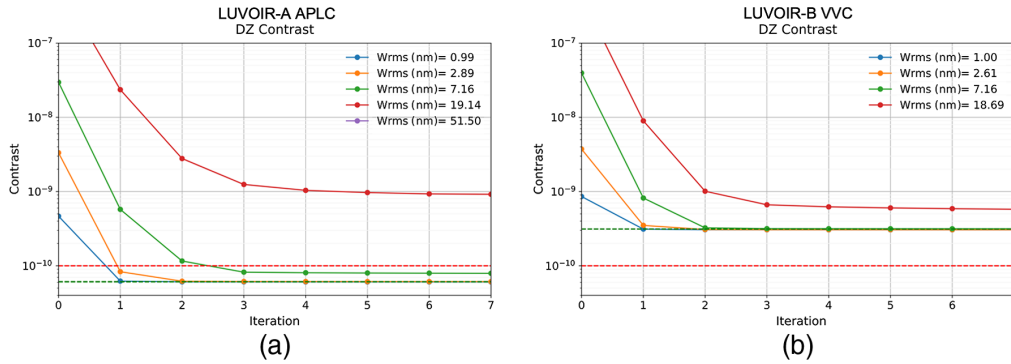


Fig. 9 Evolution of the contrast per iteration of EFC, for different levels of wavefront RMS, for (a) LUVOIR-A and (b) LUVOIR-B. EFC can correct nanometer levels of segment phasing errors. Since the DM1 is not a perfect match to the LUVOIR aperture, there is a limit to how much error the DMs can correct in broadband light. The dashed red line highlights the contrast requirement of 10^{-10} ; the dashed green line indicates the average nominal contrast of the coronagraph design.

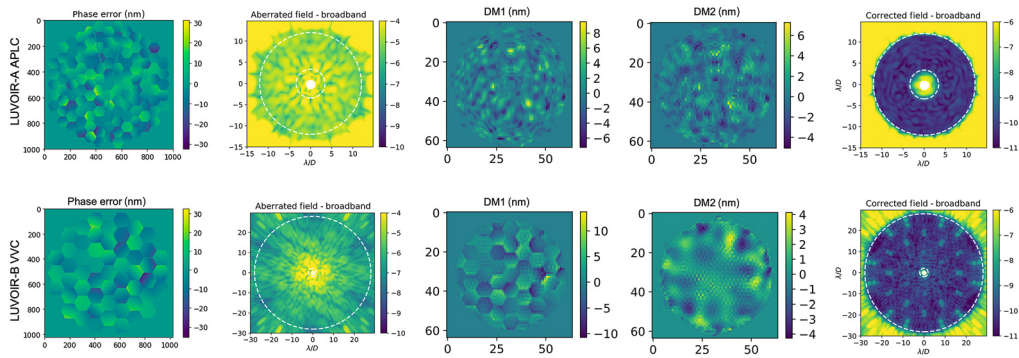


Fig. 10 Broadband (10%) wavefront error correction with EFC. Example input phase error maps for LUVOIR-A (top-left) and LUVOIR-B (bottom-left). The aberrated field shows the contrast degradation due to the wavefront errors, around five orders of magnitude for LUVOIR-A and 4 orders of magnitude for LUVOIR-B. Applying the EFC solutions for the DMs (DM1 and DM2), the nominal contrast is recovered (right) for both coronagraph designs.

Figure 10 shows the input wavefront error maps for LUVOIR-A (top-left) and LUVOIR-B (bottom-left), and the corresponding resulting aberrated PSFs before wavefront control has been applied. The initial aberrated contrast is 1.9×10^{-5} for LUVOIR-A, and 6.4×10^{-6} for LUVOIR-B. The difference in contrast resides in the OWA for both designs: for LUVOIR-A the averaged dark zone is narrower than for LUVOIR-B, capturing mainly the aberration contribution. Next, the DMs solutions are shown. For LUVOIR-B, most of the stroke is on DM1. This is because the aberrations present here are purely in phase, and DM2 is not conjugate to the pupil, as is the case with DM1. For LUVOIR-A the peak-to-valley stroke is more balanced on the two DMs because the distance between them is shorter. Note that the DM solutions for LUVOIR-B shown in Fig. 10 (bottom) do not include the initial apodizing DM shapes to clearly show the correction made by EFC, but they are added for the simulation of the corrected field [Fig. 10 (bottom-right)].

6.2 Sensitivity to Dynamic Aberrations

Once the quasi-static aberrations have been corrected with wavefront sensing and control techniques, we are left with the dynamic aberrations that are too fast for the sensing and control loop to correct. For LUVOIR, edge sensors and laser metrology systems³¹ are used to measure segment motions with picometer precision, providing a closed loop control system to maintain segment alignment stability at rates faster than can be corrected using focal plane sensing methods. In a global scale, the principal errors are expected to be in line-of-sight (LoS) pointing. Within

ECLIPS, pointing errors are sensed with the low-order or out-of-band wavefront sensor. Telescope pointing errors are also sensed by the fine guidance mode in the high definition imager (HDI). Fast pointing errors sensed by HDI are corrected by the fast steering mirror, whereas slower pointing errors are corrected at the observatory level by the vibration isolation and precision pointing system (VIPPS).³² These control loops are beyond the scope of this paper but we do quantify the effect of their residual aberrations on contrast performance.

Here, we analyze three forms of residual errors: the LoS pointing errors (Sec. 6.2.1), the dynamic segment jitter (Sec. 6.2.2), and the dynamic segment drift (Sec. 6.2.3). These are key sensitivities that will drive a complicated trade study involving integrated modeling, design reference missions, and wavefront correction to define observatory stability requirements and inform how long a science observation may be made before EFC maintenance must be done. The sensitivity analysis in this section sets limits on the jitter environment and defines a threshold where drift requires further correction with EFC to recover the required contrast. There is research being done to address the drift aspect of these dynamic aberrations^{33,34} but the analysis in this section also sets limits on jitter residuals of the observatory control and isolation systems such as the segment metrology and VIPPS.

6.2.1 Line-of-Sight pointing errors

To model the LoS pointing errors, we generate a random normal distribution of stellar offsets in the x and y direction with a given standard deviation σ_{LoS} . We have evaluated four values of σ_{LoS} : 0.1, 0.2, 0.3, and 0.5 mas. For LUVOIR, system requirements define a σ_{LoS} of 0.3 mas.

Figure 11 shows the results obtained after averaging 50 realizations per each σ_{LoS} distribution. The $\Delta\text{Contrast}$ shown is defined as the averaged PSF minus the nominal PSF. At $\sigma_{\text{LoS}} = 0.2$ mas RMS we can observe the effects of the pointing as starlight leakage in the dark zone. The effects are similar for LUVOIR-A (top row) and LUVOIR-B (bottom row), but are visually more noticeable for LUVOIR-A due to the narrower OWA. On a laboratory testbed, the RST Coronagraph team has demonstrated that a Zernike wavefront sensor can correct spacecraft LoS pointing errors to below 1-mas RMS per axis with a fast steering mirror, with a stellar flux level equivalent to apparent magnitude $V = 5$.³⁵

6.2.2 Segment phasing errors – jitter

To evaluate and quantify the system tolerance to dynamical segment phasing errors, specifically piston and tip/tilt, we have conducted a survey in which we assume eight different levels of piston and tip/tilt from 2 to 100 pm (logarithmically scaled), and we combine them. We note that the resulting sensitivities depend strongly on the telescope design and the coronagraph architecture, the number of averaged wavefront realizations, as well as the dark zone IWA.

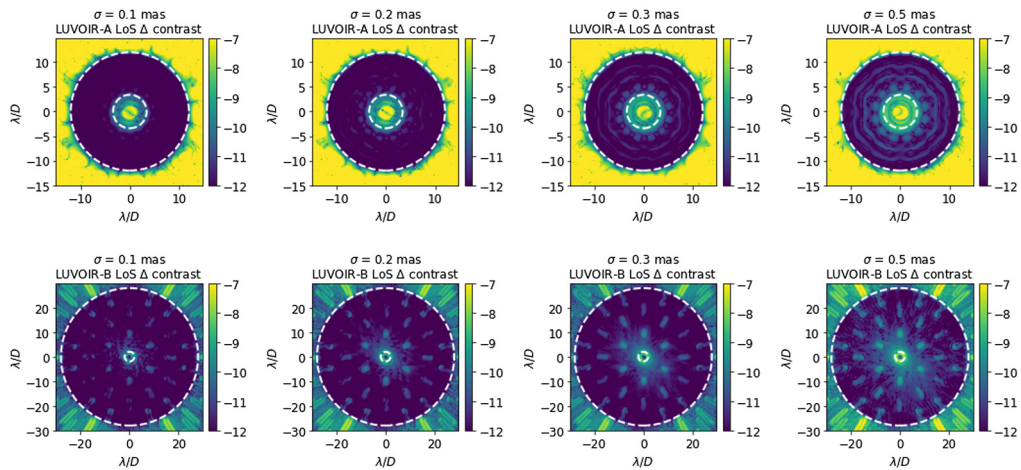


Fig. 11 Sensitivity to the LoS pointing errors for LUVOIR-A (top row) and LUVOIR-B (bottom row), for different levels of pointing errors (defined by σ_{LoS}). Each $\Delta\text{Contrast}$ is the result of averaging 50 independent wavefront realizations.

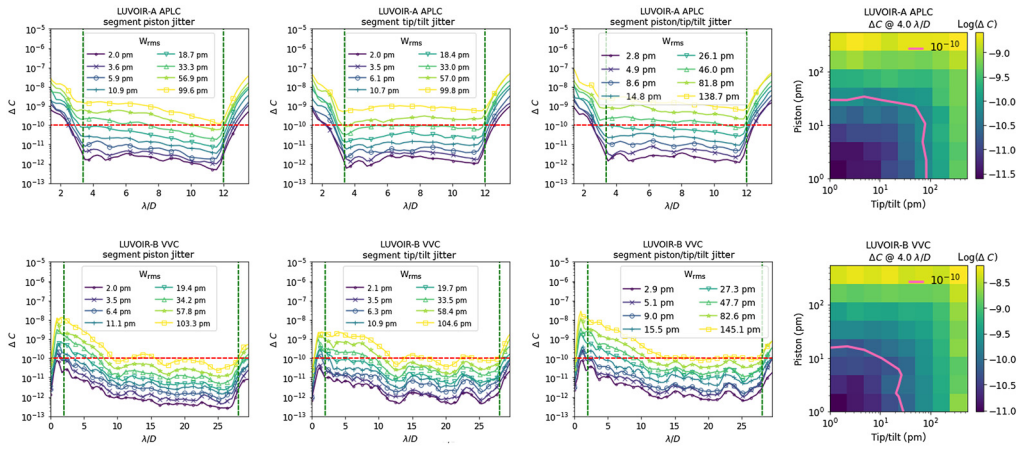


Fig. 12 Contrast degradation due to different levels of piston and tip/tilt segment jitter for LUVOIR-A (top row) and LUVOIR-B (bottom row): piston only (left), tip/tilt only (center-left), and equal levels of piston and tip/tilt (center-right). The red dashed lines are included to highlight the target contrast of 10^{-10} . The combination of piston and tip-tilt is evaluated in an $1 \lambda/D$ annulus centered at $4 \lambda/D$ from the star (right).

Figure 12 shows the results of these trials. The phase error maps are simulated assuming a normal distribution of pistons and tip/tilts across the segments with a total global RMS wavefront error ranging from 2 to 100 pm. Per each combination of piston and tip/tilt level, the contrast degradation is calculated by averaging 20 intensity maps corresponding to 20 independent realizations of piston and tip/tilt error after subtracting the nominal intensity map (error free).

For piston-dominated phase error maps (first column of plots), we observe that to remain below the raw contrast target, the wavefront RMS should not exceed a few 10 s of picometers (around 20 pm for LUVOIR-A, and around 12 pm for LUVOIR-B).

For tip/tilt dominated phase errors maps (second column of plots), the tolerance is slightly higher, specially near the IWA. When we examine the PSFs obtained after equal levels of piston and tip/tilt errors (third column of plots) are combined, the morphology of the degraded PSF is dominated by the piston contribution.

Finally, to illustrate the effect of many different combinations of piston and tip/tilt level, we evaluated the Δ Contrast for an annulus of $1 \lambda/D$ centered at $4 \lambda/D$ (right column of plots). The results are obtained after averaging 20 independent wavefront realizations. For LUVOIR-A, to achieve the raw contrast goal near the IWA, the maximum allowed wavefront RMS induced by piston and tip/tilt is around 20 and 50 pm, respectively. For LUVOIR-B, these values are around 15 pm for piston and 20 pm for tip/tilt.

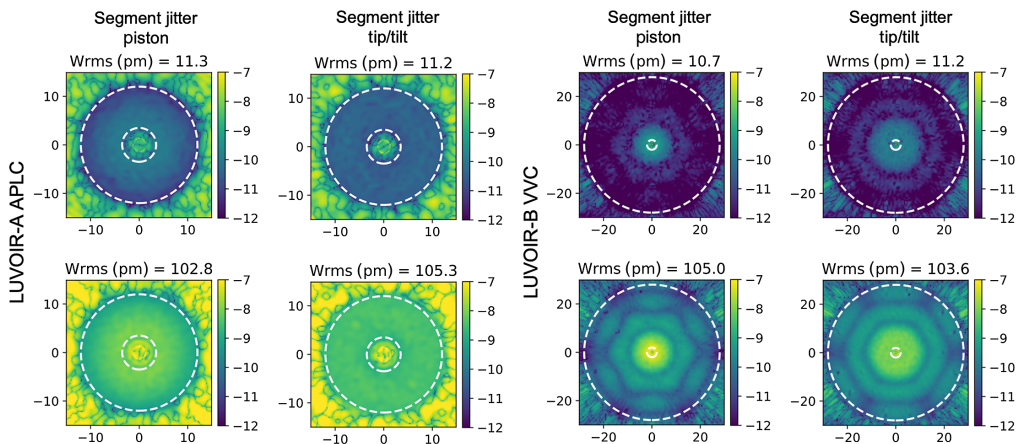


Fig. 13 Δ Contrast due to different levels of piston and tip/tilt segment jitter for LUVOIR-A (left) and LUVOIR-B (right).

Figure 13 shows examples of the final intensity maps as Δ Contrast for different levels of piston and tip/tilt segment jitter, for LUVOIR-A (left) and LUVOIR-B (right). Segment jitter has caused the speckles introduced by each realization to be averaged, hence appearing as a halo at the final intensity maps. For LUVOIR-B, we can clearly see the effects of the segmentation of the primary mirror.

6.2.3 Segment phasing errors – drift

To model the effects of segment drift, we assume the initial phase state of the primary mirror to be perfect, with zero phase errors. We then define the final phase state of the primary mirror as a normal random distribution of piston and tip/tilt values per segment. We simulate the drift by scaling the wavefront error RMS between the initial and final phase state (10 realizations), and average the resulting intensity maps. We do this for eight combinations of piston and tip/tilt values, which result in final wavefront RMS from around 3 μm up to around 150 μm .

Figure 14 shows the final intensity map in units of contrast for two examples of segment drift and the azimuthal standard deviation of various levels of drift, for LUVOIR-A (top) and

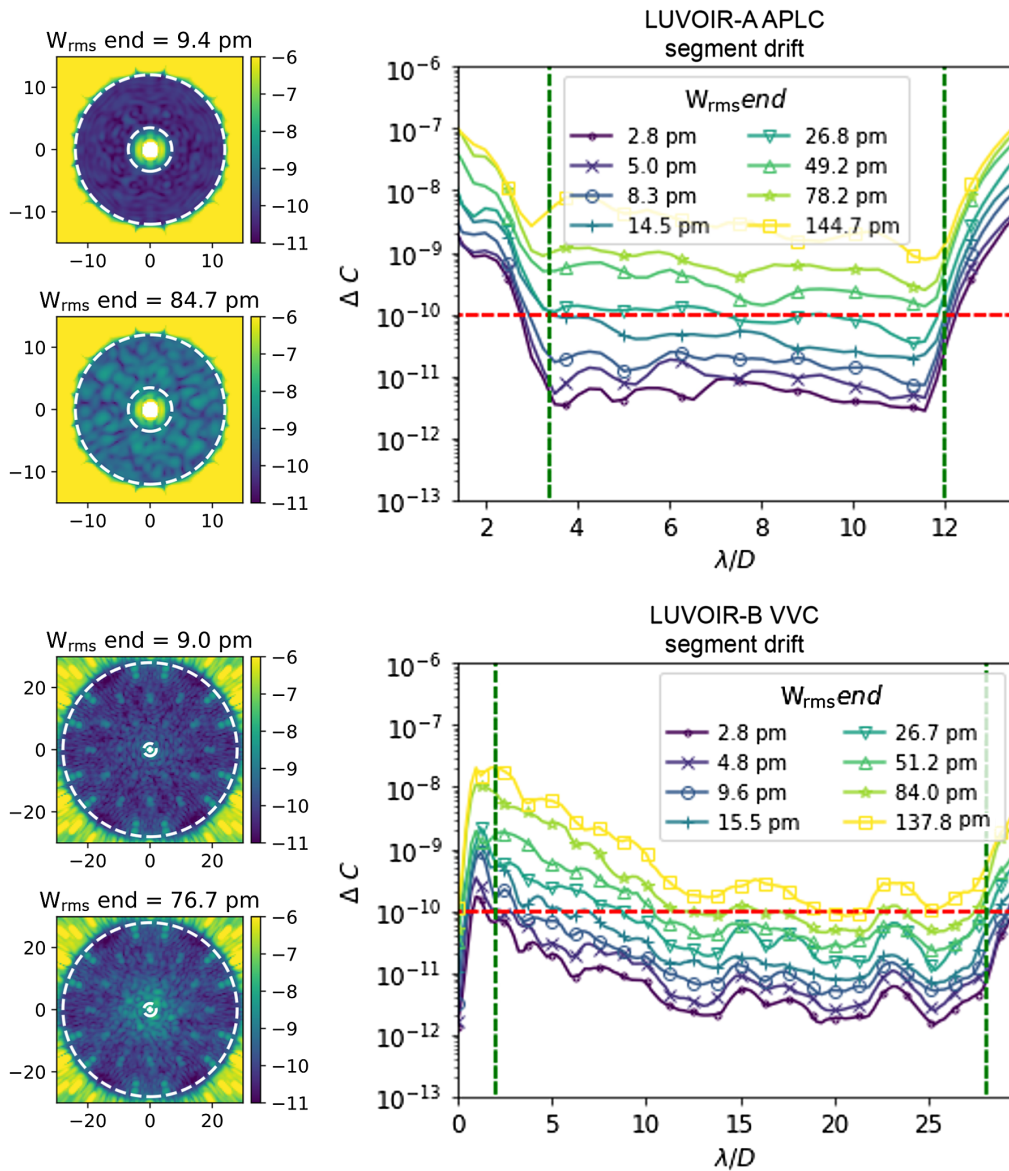


Fig. 14 Contrast degradation due to different levels of segment drift (piston plus tip/tilt) for LUVOIR-A (top) and LUVOIR-B (bottom), shown as intensity maps in units of contrast, and azimuthal standard deviation of the contrast variation Δ Contrast.

LUVOIR-B (bottom). Observing the azimuthal standard deviation of the Δ Contrast, we can see that to maintain the contrast degradation below 10^{-10} from $3.5 \lambda/D$ onward the wavefront error RMS should not surpass 10 to 15 pm when in closed loop WS&C operation.

Segment phasing drift is unique as compared to LoS and segment jitter because the speckles generated remain mostly stationary in the dark zone, compromising observations. Hence, more complex post-processing techniques will have to be used to correct for them. Interestingly, we can see that this is not an issue in the case of segment jitter shown in Fig. 13, because different speckle patterns are averaged and manifest as a halo at the final intensity map, shown there as Δ Contrast.

7 Simulated Observations

To simulate the observational capabilities of the LUVOIR-A APLC coronagraph, we use a Haystacks model of the “modern” Solar System as a test scene.³⁶ Haystacks models encode time-dependent positions and orbital phases of a given planet system architecture, with wavelength-dependent albedos, scattered light from debris structures, and background stars and galaxies. These public Solar System scene models³⁷ are stored in the form of FITS cubes containing high-resolution spatial and spectral data from 0.3 to 2.5 μm .

For the simulation shown here, we combine two LUVOIR-A APLC masks, labeled respectively narrow- and wide-angle, with respective dark zones 3.5 to $12 \lambda/D$ and 6.7 to $26.9 \lambda/D$, and respective bandpasses of 10% and 18%. We place our twin Solar System at a distance of 12.5 pc, and image the system in three bandpasses centered at 600, 700, and 800 nm. At this distance, the LUVOIR-A APLC narrow angle mask has an IWA of 0.4-AU projected separation from the star at a wavelength of 600 nm. Therefore, this observing mode can easily detect the Venus analog, as shown in Fig. 15. The OWA of the wide-angle mask simulated here translates to 3.2-AU projected separation. With this Haystack scene’s combination of observing epoch and inclination angle (60 deg), the Jupiter analog is situated near the edge of the wide-angle dark zone.

One of the essential intermediate steps in the construction of the coronagraph scene is to convolve the Haystacks irradiance distribution with the field-dependent coronagraph PSF. Figure 15 (right) shows an example for the narrow-angle mask, where the star has been removed, so that all of the intensity is due to the planets and circumstellar debris. The PSF-convolved coronagraph image is represented here in units of photon count rate on the detector and does not include any noise. The scattered light from the debris model appears as an extended, diffuse source concentrated near the edge of the APLC occulting spot.

To add the effects of residual starlight to the coronagraph image, we must set the wavefront error assumptions. First, the star is assumed to have an apparent angular diameter of 0.75 mas, consistent with a G-dwarf at the 12.5-pc target distance. We assume the residual RMS LoS

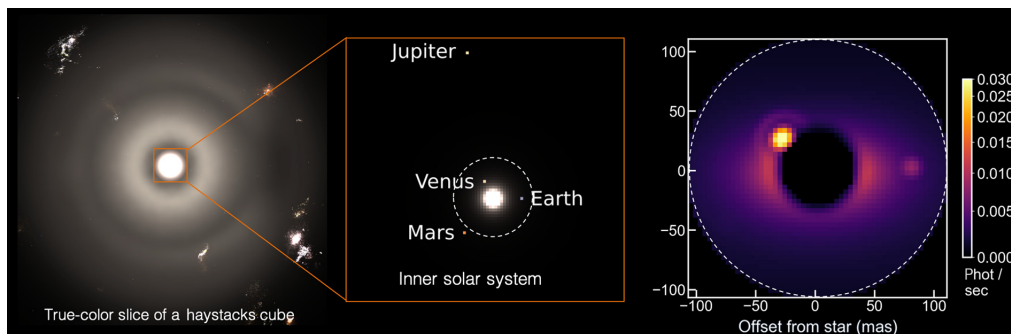


Fig. 15 True color image generated from our high-fidelity model of the face-on modern solar system (left), showing the entire field-of-view. The center panel zooms in on the inner system where for ease of viewing, the Sun and background sources were not included. The bright region at the center of the image (left) is emission from exozodiacal dust. The partial ring in the outer dust structure is caused by the dynamical influence of Neptune. The planets occupy single pixels and are not readily apparent in the larger image without zooming in. The LUVOIR-A APLC narrow angle masks, delimited by the white dashed circle, allow the detection of Venus and Earth (right).

pointing error is 0.2 mas, which is combined with a primary segment jitter (piston and tip/tilt) that introduces a total wavefront error RMS of ~ 10 -pm per instantaneous realization. To simulate the time series, we average the intensity maps resulting from 50 independent realizations of segment phasing errors and LoS pointing errors distributions.

To enable differential imaging to mitigate the residual starlight as well as scattered light from the exozodiacal dust, we simulate images acquired at two observatory roll angles spaced apart by 27 deg. Later, we apply simple roll subtraction to the noisy co-added images.

Figure 16 shows the images obtained in each wavelength channel, after detector noise has been included and roll-subtraction has been performed. We assumed values of quantum efficiency (QE), dark current, and read noise consistent with the electron multiplying charge-coupled device (EMCCD)³⁸ design parameters baselined for ECLIPS. The total integration time is 60-h split in 17, 19, and 24 h for the 600-, 700-, and 800-nm channel, respectively. This total integration time, which includes the observation with the two APLC masks and the two observatory rolls per channel, also includes 25% overheads to account for cosmic ray data losses. No other overheads have been included. The wavelength dependence in the IWA and OWA can be clearly seen: for the 600-nm channel, the wide angle masks can observe Jupiter only partially, whereas for the 800-nm channel Venus has been attenuated by the occulting mask. Earth is detected in each of the wavelength channels with a signal-to-noise ratio (SNR) of 14, 12, and 9 at 600, 700, and 800 nm, respectively. The respective SNRs of the Venus- and Jupiter-analog point sources are $\sim 15\times$ and $30\times$ higher than the Earth-analog in each image where they appear in the field-of-view.

Multi-band photometry at these SNRs would give evidence that the Earth-analog point source is a planet and not a background star. With the addition of mass constraints from radial velocity or precision reflex motion astrometry,³⁹ the photometry would constrain the bulk geometric albedo. The same constraints, or relative astrometry from follow-up epochs, would establish the planet's orbital separation in relation to the host star's habitable zone.

Maintaining this level of coronagraph performance over yet longer integration times would enable observers to begin spectroscopically characterizing the Earth analog's atmosphere. Simulations of atmospheric retrieval^{40,41} showed that a visible wavelength spectrum (in the the LUVOIR and Habitable Exoplanet Observatory concepts, obtained with an integral field spectrograph situated behind the coronagraph), at an SNR of 10 per spectral bin at resolution $R = 140$, would be sufficient to detect the presence of O_2 in the atmosphere of a modern Earth analog. The broader water vapor absorption feature at 940 nm would be detected with an SNR of 5 per bin at a spectral resolution of $R = 70$.

Finally, we combined the reduced coronagraph images from the three bandpasses from Fig. 16 to generate the RGB composite shown in Fig. 17. The colors at the edge of the field-of-view illustrate the dependence of OWA on wavelength. While this data simulation is preliminary and not based on a fully integrated structural-thermal-optical performance model, it gives us confidence that a mission such as LUVOIR could detect exo-Earths around nearby stars with high enough SNR to perform spectroscopy and characterize their atmospheres.

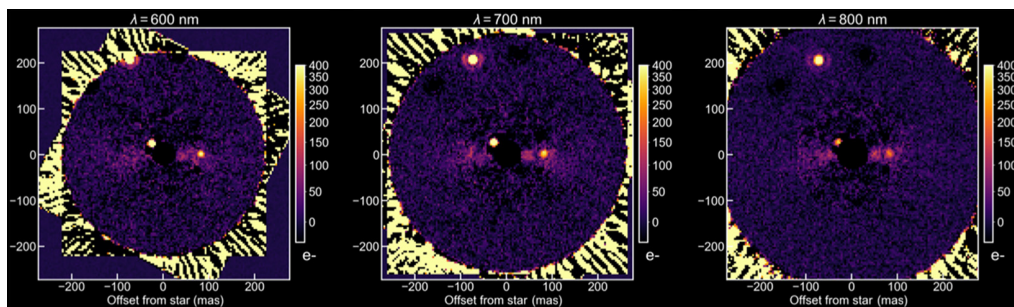


Fig. 16 Coronagraph images for the 600-nm bandpass (left), 700-nm bandpass (center) and 800-nm bandpass (right). The total integration time is 60 h and includes 25% overheads, and is distributed as: 17 h for the 600-nm bandpass (5 h for the APLC narrow angle mask and 3 h for the APLC wide angle mask, repeated at two rolls), 19 h for the 700-nm bandpass (6 h for the APLC narrow angle mask and 3 h for the APLC wide angle mask, repeated at two rolls) and 24 h for the 800-nm bandpass (8 h for the APLC narrow angle masks and 4 h for the APLC wide angle masks).

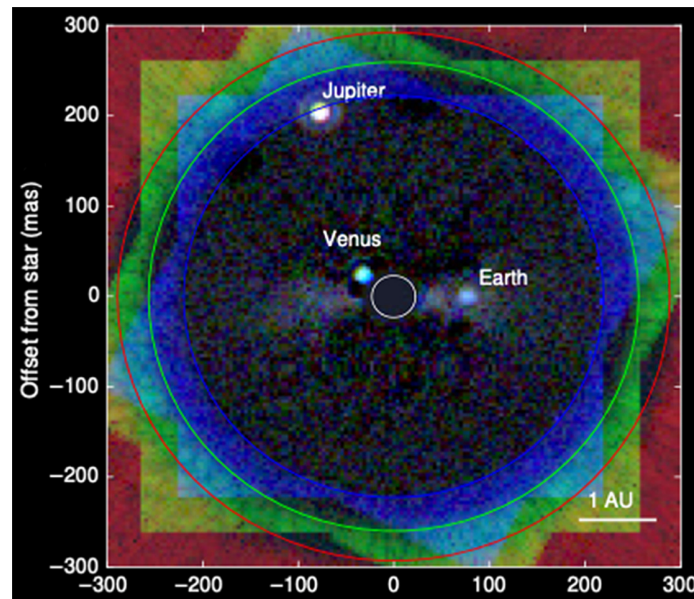


Fig. 17 Simulated image of a twin Solar System at a distance of 12.5 pc observed through the LUVOIR-A ECLIPS instrument. This RGB image is a composite of data acquired in two APLC masks (with respective working angles $3.5 - 12 \lambda/D$ and $7 - 27 \lambda/D$) in three bandpasses (red—800 nm; green—700 nm; and blue—600 nm) at two observatory roll angles (27 deg apart) over the course of 60 h of total integration time. The coronagraph images were simulated with a diffraction model time series that includes 10 pm of primary mirror segment jitter (random piston and tip-tilt errors applied to each mirror segment), 0.2-mas residual LoS pointing jitter, and a stellar diameter of 0.75 mas. The input astrophysical scene is a model of a modern Solar System inclined at 60 deg, with an exozodiacal debris disk. In this scene, the Earth-like planet is observed at quadrature, appearing as a blue dot at 1-AU projected separation, to the right of the occulted star. Roll subtraction processing was used to remove starlight speckles from the raw co-added images. The residual structure of the exozodiacal disk—distorted by the roll subtraction – appears as a horizontally extended diffuse cloud.

8 Conclusions

In this paper, we have presented the coronagraph designs envisioned for the LUVOIR-A and LUVOIR-B ECLIPS instrument, an APLC and VVC, respectively, and evaluated their performance in terms of contrast, core throughput, distortion near the IWA, sensitivity to stellar diameter and sensitivity to telescope aberrations. Both designs offer similar performance in terms of sensitivity to stellar angular size and wavefront errors.

We performed a systematic aberration sensitivity analysis, evaluating both global and segment-level wavefront errors, for quasi-static and dynamic cases. By simulating the full high-order wavefront sensing and control loop, we conclude that ECLIPS can compensate for quasi-static wavefront aberrations up to several nanometers due to segment level phasing errors. All the simulations presented here assume a 10% instantaneous bandpass, which for LUVOIR-A is defined by the coronagraph mask design. The wavefront sensing and control system does not limit the bandpass, hence future coronagraph masks designs that increase the bandpass could improve the coronagraph performance by reducing the filter requirements and the total observing time, consequently. With respect to dynamic wavefront aberrations, both designs maintain their target contrast of 10^{-10} with segment jitter wavefront error levels in the range 15- to 20-pm RMS after closed-loop wavefront sensing and control.

Finally, we have presented the first LUVOIR ECLIPS data simulations incorporating error sources consistent with the engineering requirements defined in the LUVOIR study report. Under our present assumptions for residual dynamical wavefront errors, simulations suggest that simple roll subtraction is an effective means to recover exoplanet point sources at 10^{-10} contrast in the habitable zones of nearby stars. We will continue to investigate various levels and combinations of telescope wavefront errors and drifts, as well as instrument optical train aberrations.

Future work will extend the simulations to include integral field spectroscopy data and retrieval of planet atmospheric properties.

Acknowledgments

R. Juanola-Parramon was supported by NASA through the CRESST II cooperative agreement CA 80GSFC17M0002 and by NASA Exoplanet Exploration Program's (ExEPs) Segmented Coronagraph Design and Analysis (SCDA) study. The authors would like to thank Dr. Rémi Soummer of STScI for the LUVOIR-A APLC coronagraph designs and the LUVOIR Study Team.

References

1. N. A. of Sciences Engineering and Medicine, *Exoplanet Science Strategy*, The National Academies Press, Washington, DC (2018).
2. National Academies of Sciences, Engineering, and Medicine. *Pathways to Discovery in Astronomy and Astrophysics for the 2020s*, The National Academies Press, Washington, DC (2021).
3. The LUVOIR Team, "The LUVOIR mission concept study final report," arXiv:1912.06219 (2019).
4. K. France et al., "The LUVOIR Ultraviolet Multi-Object Spectrograph (LUMOS): instrument definition and design," *Proc. SPIE* **10397**, 1039713 (2017).
5. E. Muslimov et al., "POLLUX: a UV spectropolarimeter for the LUVOIR space telescope project," *Proc. SPIE* **10699**, 1069906 (2018).
6. L. Pueyo et al., "The LUVOIR architecture "A" coronagraph instrument," *Proc. SPIE* **10398**, 103980F (2017).
7. L. Pueyo et al., "The LUVOIR Extreme Coronagraph for Living Planetary Systems (ECLIPS) I: searching and characterizing exoplanetary gems," *Proc. SPIE* **11117**, 37–65 (2019).
8. R. Juanola-Parramon et al., "The LUVOIR Extreme Coronagraph for Living Planetary Systems (ECLIPS) II. Performance evaluation, aberration sensitivity analysis and exoplanet detection simulations," *Proc. SPIE* **11117**, 21–36 (2019).
9. C. C. Stark et al., "Exoearth yield landscape for future direct imaging space telescopes," *J. Astron. Telesc. Instrum. Syst.* **5**(2), 024009 (2019).
10. <https://exoplanets.nasa.gov/exep/technology/SCDA/>.
11. S. Shaklan et al., "Status of space-based segmented-aperture coronagraphs for characterizing exo-earths around sun-like stars," *Bulletin of the American Astronomical Society* **51**(7), 211 (2019).
12. R. Soummer, C. Aime, and P. E. Falloon, "Stellar coronagraphy with prolate apodized circular apertures," *Astron. Astrophys.* **397**, 1161–1172 (2003).
13. M. N'Diaye et al., "Apodized pupil lyot coronagraphs for arbitrary apertures. V. Hybrid shaped pupil designs for imaging earth-like planets with future space observatories," *Astrophys. J.* **818**, 163 (2016).
14. N. T. Zimmerman et al., "Lyot coronagraph design study for large, segmented space telescope apertures," *Proc. SPIE* **9904**, 99041Y (2016).
15. G. Foo, D. M. Palacios, and G. A. Swartzlander, "Optical vortex coronagraph," *Opt. Lett.* **30**(24), 3308–3310 (2005).
16. D. Mawet et al., "Annular groove phase mask coronagraph," *Astrophys. J.* **633**(2), 1191 (2005).
17. O. Guyon et al., "Exoplanet imaging with a phase-induced amplitude apodization coronagraph. I. Principle," *Astrophys. J.* **622**(1), 744 (2005).
18. O. Guyon et al., "High performance lyot and pisa coronagraphy for arbitrarily shaped telescope apertures," *Astrophys. J.* **780**(2), 171 (2014).
19. R. Belikov et al., "Design and performance analysis of a piaacmc coronagraph on a segmented aperture," *Proc. SPIE* **10698**, 106981H (2018).

20. C. C. Stark et al., “Maximizing the exoearth candidate yield from a future direct imaging mission,” *Astrophys. J.* **795**, 122 (2014).
21. Q. Gong et al., “Optical design of the extreme coronagraph for living planetary systems instrument for the LUVOIR mission study,” *J. Astron. Telesc. Instrum. Syst.* **5**(2), 1–13 (2019).
22. N. T. Zimmerman et al., “Shaped pupil Lyot coronagraphs: high-contrast solutions for restricted focal planes,” *J. Astron. Telesc. Instrum. Syst.* **2**, 011012 (2016).
23. J. Mazoyer et al., “Active correction of aperture discontinuities-optimized stroke minimization. II. Optimization for future missions,” *Astron. J.* **155**(1), 8 (2018).
24. G. Ruane et al., “Fast linearized coronagraph optimizer (FALCO) IV: coronagraph design survey for obstructed and segmented apertures,” *Proc. SPIE* **10698**, 106984U (2018).
25. J. E. Krist, “Proper: an optical propagation library for IDL,” *Proc. SPIE* **6675**, 66750P (2007).
26. R. Soummer et al., “Fast computation of lyot-style coronagraph propagation,” *Opt. Express* **15**, 15935–15951 (2007).
27. Q. Gong et al., “Optical design of exo-planet coronagraph, integral field spectrograph, and high resolution spectrometer for luvoir study (conference presentation),” *Proc. SPIE* **10698**, 1069812 (2018).
28. B. Nemati et al., “The effects of space telescope primary mirror segment errors on coronagraph instrument performance,” *Proc. SPIE* **10398**, 103980G (2017).
29. R. Juanola-Parramon et al., “Evaluating the luvoir coronagraph sensitivity to telescope aberrations,” in *IEEE Aerosp. Conf.*, pp. 1–8 (2019).
30. A. Give’on, B. D. Kern, and S. Shaklan, “Pair-wise, deformable mirror, image plane-based diversity electric field estimation for high contrast coronagraphy,” *Proc. SPIE* **8151**, 815110 (2011).
31. J. Z. Lou et al., “LUVOIR primary mirror segment alignment control with joint laser metrology and segment edge sensing,” *Proc. SPIE* **10698**, 1184–1197 (2018).
32. L. D. Dewell et al., “Dynamic wavefront error and line-of-sight performance predictions for the 15-meter segmented Large Ultraviolet/Optical/Infrared Surveyor (LUVOIR) with non-contact vibration isolation,” *Proc. SPIE* **11115**, 111150S (2019).
33. L. Pogorelyuk and N. J. Kasdin, “Dark hole maintenance and a posteriori intensity estimation in the presence of speckle drift in a high-contrast space coronagraph,” *Astrophys. J.* **873**(1), 95 (2019).
34. K. Miller, O. Guyon, and J. Males, “Spatial linear dark field control: stabilizing deep contrast for exoplanet imaging using bright speckles,” *J. Astron. Telesc. Instrum. Syst.* **3**(4), 049002 (2017).
35. F. Shi et al., “WFIRST low order wavefront sensing and control dynamic testbed performance under the flight like photon flux,” *Proc. SPIE* **10698**, 825–842 (2018).
36. A. Roberge et al., “Finding the needles in the Haystacks: high-fidelity models of the modern and archean solar system for simulating exoplanet observations,” *Publ. Astron. Soc. Pacific* **129**(982), 124401 (2017).
37. <https://asd.gsfc.nasa.gov/projects/haystacks>.
38. L. K. Harding et al., “Technology advancement of the CCD201-20 EMCCD for the WFIRST coronagraph instrument: sensor characterization and radiation damage,” *J. Astron. Telesc. Instrum. Syst.* **2**(1), 011007 (2016).
39. M. Shao et al., “Finding exo-Earths with precision space astrometry,” *Bull. Am. Astron. Soc.* **51**(3), 74 (2019).
40. Y. K. Feng et al., “Characterizing earth analogs in reflected light: atmospheric retrieval studies for future space telescopes,” *Astron. J.* **155**(5), 200 (2018).
41. M. Damiano and R. Hu, “Reflected spectroscopy of small exoplanets II: characterization of terrestrial exoplanets,” *Astron. J.* **163**(6), 299 (2022).

Roser Juanola-Parramon received her BS and MS degrees in electrical engineering and computer science, and her MS degree in photonics from Polytechnic University of Catalonia, Spain, in 2008, and her PhD in astrophysics in 2014 from the University College London,

United Kingdom. She is currently a research engineer at NASA Goddard Space Flight Center. Her current research activities include modeling coronagraph instruments and corresponding wavefront sensing and control.

Neil T. Zimmerman is a research astrophysicist in the Exoplanets and Stellar Astrophysics Laboratory at NASA's Goddard Space Flight Center. He is a member of the Nancy Grace Roman Space Telescope Project Science team, and his research encompasses coronagraph design and simulation, data processing techniques, and spectroscopy technologies for future exoplanet imaging missions.

Laurent Pueyo is an astronomer at the Space Telescope Science Institute in Baltimore, Maryland. He earned his doctorate from Princeton University in 2008 and conducted his post doctoral work as a NASA Fellow at the Jet Propulsion Laboratory and as a Sagan Fellow at the Johns Hopkins University.

Matthew Bolcar is an optical systems engineer at NASA's Goddard Space Flight Center. He is currently the lead optical systems engineer for NASA's Roman Space Telescope (formerly WFIRST). Prior to that, he was the lead engineer for the Large Ultraviolet-Optical-Infrared Surveyor (LUVOIR) Decadal Mission Concept Study, for which he also co-chaired the Technology Working Group. He received a BS degree in engineering physics from Cornell University in 2002 and a PhD in optics from the University of Rochester in 2009.

Qian Gong is a research optical engineer at NASA Goddard Space Flight Center. She received her PhD from Optical Sciences Center, University of Arizona, in 1990. She is on a Goddard research engineering partnership program to work with scientists for developing innovative concept design to achieve challenging science goals. Meanwhile, she also designed Roman Space Telescope grism and prism spectrometers and CGI integral spectrograph. Prior to that, she has worked on HST, JWST, and many other projects as an optical engineer or optics lead.

Tyler Groff received his bachelor's degree in mechanical engineering and astrophysics in 2007 from Tufts University and his PhD in mechanical and aerospace engineering from Princeton University in 2012. His research focuses on visible and near-infrared instrumentation for exoplanet science, coronagraph design, and wavefront control. He is the lead engineer at Goddard for the Roman Space Telescope CGI prism and polarizer modes.

John Krist is a research scientist at the Jet Propulsion Laboratory and leads the Roman Space Telescope Coronagraph integrated modeling team. He is also associated with JWST NIRC2 science team, specifically with the coronagraph. He was previously an optical analyst at the Space Telescope Science Institute.

Aki Roberge is a research astrophysicist at Goddard Space Flight Center and she was the study scientist for the LUVOIR Decadal Survey Mission Concept Study. Her research focuses the study of planet formation through multi-wavelength observations of circumstellar disks around nearby young stars and the development of future exoplanet mission concepts.

Garreth Ruane is an optical engineer at NASA's Jet Propulsion Laboratory working on astronomical instrumentation, especially for high contrast imaging and characterization of exoplanets. He is involved in the development of the high contrast modes for Keck/NIRC2 and the Keck planet imager and characterizer (KPIC). He received his PhD from Rochester Institute of Technology in 2016 and was an NSF Astronomy and Astrophysics postdoctoral fellow at Caltech from 2016 to 2019.

Christopher Stark is a research astrophysicist at Goddard Space Flight Center and the deputy integration, test, and commissioning project scientist for the James Webb Space Telescope. His research includes science yield studies for future direct imaging mission concepts, high-contrast observations of debris disks, and theoretical modeling of dust dynamics and disk-planet interactions.